Research article

Insights into the mechanism of persulfate activation with biochar composite loaded with Fe for 2,4-dinitrotoluene degradation

Xiaodong Li [1], Huizhen Cao [1], Yuan Cao, Yao Zhao, Wenwen Zhang, Jialun Shen, Zongquan Sun, Fujun Ma [**], Qingbao Gu [*]

State Key Laboratory of Environmental Criteria and Risk Assessment, Chinese Research Academy of Environmental Sciences, Beijing, 100012, China

ARTICLE INFO

ABSTRACT

Iron in biochar composite loaded with Fe (Fex@biochar) is crucial for persulfate activation. However, the iron dosages-driven mechanism linked to the speciation, electrochemical property, and persulfate activation with Fex@biochar remains ambiguous. We synthesized and characterized a series of Fex@biochar and evaluated its catalytic performance in 2,4-dinitrotoluene removal experiments. With increasing $FeCl_3$ dosage, iron speciation in Fex@biochar changed from γ-Fe_2O_3 to Fe_3O_4, and the variation in functional groups was as follows: Fe–O, aliphatic C–O–H, O–H, aliphatic C–H, aromatic C=C or C=O, and C–N. The electron accepting capacity of Fex@biochar increased as the $FeCl_3$ dosage increased from 10 to 100 mM but decreased at 300 and 500 mM $FeCl_3$. 2,4-dinitrotoluene removal first increased and subsequently decreased, reaching 100% in the persulfate/Fe100@biochar system. The Fe100@biochar also showed good stability and reusability for PS activation, verified by five test cycles. The mechanism analysis indicated that the iron dosage altered the Fe (III) content and electron accepting capacity of Fex@biochar during pyrolysis, further controlling persulfate activation and 2,4-dinitrotoluene removal. These results support the preparation of eco-friendly Fex@biochar catalysts.

1. Introduction

In situ chemical oxidation (ISCO) is one of the most commonly observed groundwater remediation technologies. It mainly adopts oxidants with strong oxidation abilities, such as potassium permanganate, hydrogen peroxide (H_2O_2), and persulfate (PS), to degrade organic contaminants in groundwater into non-toxic or low-toxic substances (Wei et al., 2022a). Potassium permanganate reacts quickly with organic contaminants but possibly clogs soil pores because of manganese dioxide formation, affecting the transport of oxidants (Poulson and Naraoka, 2002). Although H_2O_2 can quickly generate ●OH, the reaction conditions are strictly acidic (pH < 3), which leads to increased treatment costs (Bokare and Choi, 2014). The PS oxidation system has developed into a significant branch of ISCO because its cost ($0.74/kg PS) is lower than that of H_2O_2 ($1.5/kg H_2O_2) and because of its convenient storage and transportation (Zhang et al., 2016b). Appropriate activation methods with PS oxidation can efficiently degrade organic

contaminants. In the context of green and sustainable remediation, biochar composites loaded with Fe (Fex@biochar) are widely used to remediate contaminated groundwater because of their environmental friendliness, broad availability of feedstocks, and potential benefits to the circular economy (Yang et al., 2022; Lyu et al., 2020; He et al., 2022a). Particularly, Fex@biochar is rich in defects, oxygen functional groups, and a spectrum of iron species; thus, Fex@biochar is commonly used as an activator of PS base ISCO for organically contaminated groundwater (Fang et al., 2015).

Iron speciation is assumed to be the most important redox-active component of Fex@biochar (Ling and Zhang., 2017; Xu et al., 2021). The carbon phase acts as a support substrate via physicochemical effects to disperse and fix iron particles in Fex@biochar and offers substantial electron transfer reactivity (Li et al., 2020a; Xu et al., 2022). The different speciation of iron and carbon resulted in various electrochemical properties of the Fex@biochar, which sustained diverse redox-related remediation processes. For example, Wang et al. (2020)

---

found that containing-Fe^0 functional group is a major factor in determining the electron transport capacity of biochar. Yu et al. (2021) reported that the presence of a C=C bond could improve the electron donation capacity (EDC) of biochar, further enhancing PS activation and organic contaminant degradation. Studies have reported that Fe dosages on the surface of biochar could affect the Fe content and carbon speciation in Fex@biochar (Song et al., 2021b; Guo et al., 2022). The researchers explored the surface morphology, crystalline structure, and interfacial chemical behavior of a series of Fex@biochar and revealed the influence of the Fex@biochar structure on the adsorption and immobilization of pollutants (Sun et al., 2019, 2022b; Xu et al., 2022). For example, Sun et al. (2019) reported that Fex@biochar prepared by pyrolysis exhibited a high removal capacity for inherent cations by bridging with C=O bonds and cation-π interactions. In summary, the literature has mainly investigated the adsorption and stabilization performance of Fex@biochar at high pyrolysis temperatures for pollutants, with few studies on the activation efficiency of low-pyrolysis-temperature (< 400 °C) biochar for PS. The Fe dosage-driven response relationship based on iron and carbon speciation, electrochemical properties, and PS activation requires further investigation using complementary characterization methods.

Speciation transformation of Fex@biochar during pyrolysis mainly includes the changes in crystalline, chemical structural components, and functional groups, which can be well described by X-ray diffraction (XRD), X-ray photoelectron spectroscopy (XPS), and Fourier transform infrared spectrometry (FTIR) (Guo et al., 2020; Wang et al., 2021). Two-dimensional correlation spectroscopy (2D COS) possibly converted spectral matrix and has been employed to recognize the relative directions and specific sequences of speciation transformation in biochar in response to the pyrolysis temperature (Song et al., 2021a; Li et al., 2023; Ruan et al., 2023). However, few studies have explored the response of sequential variations in iron and carbon speciation in Fex@biochar to iron dosage during pyrolysis. Joint 2D COS analyses can facilitate a holistic understanding of the mechanism of speciation transformation in Fex@biochar during pyrolysis (Song et al., 2019). An electrochemical workstation is usually used to determine the electrochemical properties (EDC and electron accepting capacity (EAC)) of Fex@biochar (Sun et al., 2022a). Therefore, the combination of modern characterization methods is useful for constructing an iron dosage-driven response relationship and illustrating the mechanism of PS activation by Fex@biochar at different Fe dosages.

In this study, the mechanism linking the speciation transformation, electrochemical properties, and PS activation with Fex@biochar was elucidated using modern characterization methods combined with 2D COS and statistical analysis. 2,4-dinitrotoluene (2,4-DNT), a common refractory pollutant in groundwater (Amaral et al., 2009), was selected as the targeted contaminant to evaluate the catalytic performance of Fex@biochar. The objectives were to (1) characterize the speciation transformation (crystalline, chemical structural components, and functional groups) and electrochemical properties of Fex@biochar with an increase in Fe dosage during pyrolysis; (2) evaluate the performance of Fex@biochar-activated PS oxidation by conducting removal experiments and electron spin resonance (ESR) analysis; and (3) establish a response relationship based on iron and carbon speciation, electrochemical properties, and PS activation using Pearson correlation coefficient analysis and provide direct evidence for the underlying mechanism of PS. The results of this study are expected to provide a new strategy for optimizing the preparation and catalytic performance of Fex@biochar.

2. Materials and methods

Corn straw biochar has a diverse and large number of functional groups, which is inversely proportional to the pyrolysis temperature (Yuan et al., 2011; Xing et al., 2018). He et al. (2022c) found that the number of carboxyl functional groups in corn straw biochar was higher

than that in rapeseed straw biochar. In this study, we selected corn straw biomass, a common agricultural residue in China, as the biochar feedstock, impregnated it with an inexpensive and easily available FeCl$_3$ solution, and prepared Fex@biochar by impregnation and pyrolysis. Specifically, corn straw (10.0 g) passing through 10 sieve mesh was first impregnated into 1 L deionized water with different dosages of FeCl$_3$·6H$_2$O (0, 10, 50, 100, 300, and 500 mM), stirred at 25 °C for 12 h (Yi et al., 2020). During this process, the solution pH was not adjusted, and the values were 6.15, 6.26, 6.34, 6.15, and 6.34, respectively. After removing the supernatant and drying at 90 °C, the impregnated corn straw was put into a tube furnace, and the pyrolysis temperature raised from 25 °C to 300 °C at 10 °C min^{-1} of pyrolysis rate and 0.5 L min^{-1} of nitrogen flow (Continue to stay at 300 °C for 3 h). The Fex@biochar passed through a 100-sieve mesh in subsequent experiments. When the FeCl$_3$ impregnation concentration is 10, 50, 100, 300, and 500 mM, and the Fe dosages on Fex@biochar were 37.6, 87.8, 127.5, 190.7, and 211.3 mg g^{-1}, respectively. Preliminary experimental results showed that when the pyrolysis temperature, retention time, and heating rate was retained at 300 °C, 3 h, and 10 °C·min^{-1}, respectively, the PS/Fe10@biochar oxidation system exhibited an excellent removal for 2,4-DNT (Fig. S1, Table S1, and Text S1). The characterization methods of corn straw and Fex@biochar were described in Text S2. The catalytic removal experiments of Fex@biochar were conducted in a centrifuge tube, and the detailed description can be found in Text S3.

3. Results and discussion

3.1. Speciation transformation of biochar composite loaded with Fe

3.1.1. Crystalline phases

The XRD patterns of Fex@biochar with different FeCl$_3$ dosages are illustrated in Fig. 1a, and all exhibit pronounced diffraction peaks of FeCl$_2$·4H$_2$O, graphite C, Fe$_2$O$_3$, and Fe$_3$O$_4$. FeCl$_2$·4H$_2$O diffraction peaks at 2θ = 16.102°, 22.376°, and 41.344° were observed for all Fex300-biochar and Fex500biochar (PDF#16–0123). Graphite C (26.611°) was observed in Fex50biochar and Fex100biochar. A Fe$_3$O$_4$ diffraction peak at 2θ = 35.482° was observed for all Fex@biochar samples except for Fe10@biochar (PDF#75–0033). The diffraction peaks at 2θ = 30.124° and 42.123° were identified as the (2 2 0) and (4 0 0) planes of Fe$_3$O$_4$, respectively (PDF#75–0033) (Wang et al., 2023). The peaks at 2θ = 32.641° and 35.092° matched the (1 0 11) and (2 0 1) planes of Fe$_2$O$_3$, respectively, which all appeared in Fe300@biochar and Fe500@biochar (PDF#40–1139). We concluded that the intensities of the Fe$_2$O$_3$ and Fe$_3$O$_4$ peaks significantly increased when the FeCl$_3$ dosage was increased from 10 to 500 mM, suggesting that the content and crystallinity of FeO$_x$ in Fex@biochar increased, in accordance with the literature (Zhang et al., 2020). The iron phases in Fex@biochar were also observed using SEM-EDS (Fig. S2). At FeCl$_3$ dosages of 10, 50, 100, 300, and 500 mM, the Fe contents on the surface of the Fex@biochar were 0.81%, 3.83%, 10.05%, 15.16%, and 17.63%, respectively. The average particle sizes of Fe minerals were calculated at a magnification of 50,000 times and decreased from 251.2 to 102.8 nm, and a similar result was reported in the previous study (Niznansky et al., 1997).

3.1.2. Sequential responses of functional groups

The functional groups in Fex@biochar were monitored by FTIR spectra, namely including O–H stretching vibration (3451 cm^{-1}), aliphatic C–H stretching vibration (2918 cm^{-1}), aromatic C=C or C=O stretching vibrations (1610–1615 cm^{-1}), C–N bending vibration (1500 cm^{-1}), aliphatic C–O–H stretching vibration (1059 cm^{-1}) (Fig. 1b). In addition, an Fe–O bond (561 cm^{-1}) was produced in Fex@biochar, suggesting the formation of iron oxides on the surface of Fex@biochar during pyrolysis (Yang et al., 2016; Hou et al., 2018). With an increase in the FeCl$_3$ dosage, the strength of the bands for the functional groups increased, demonstrating that the addition of iron possibly facilitated the formation of external oxygen functional groups. Zhang et al. (2020)
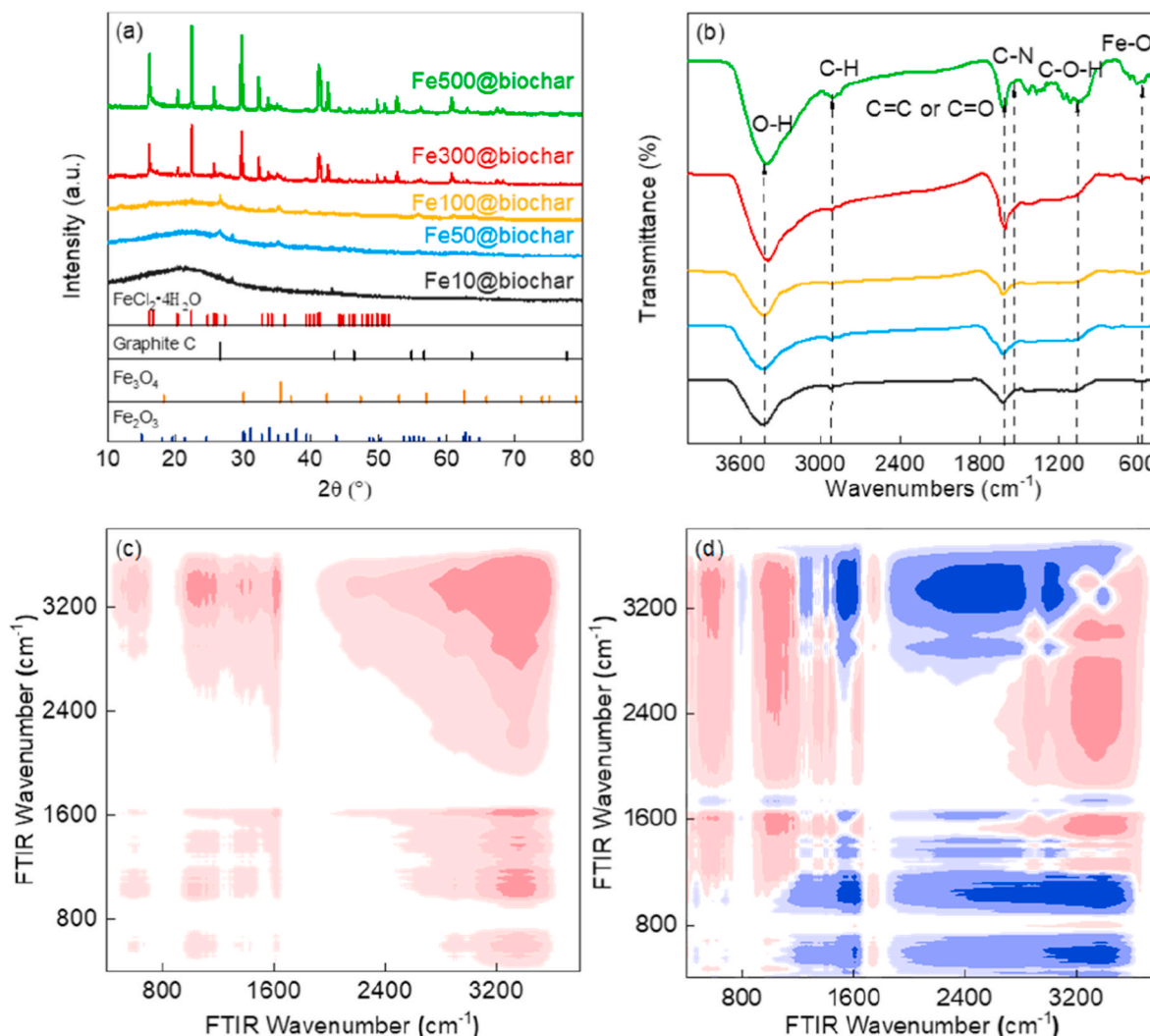
Fig. 1. Speciation transformation of Fex@biochar prepared by different FeCl$_3$ dosages. XRD (a); FTIR spectra (b); Synchronous (c) and asynchronous (d) of 2D COS maps generated from the FTIR spectra. Red and blue represent positive and negative correlation, respectively.

found that the intensity of the O–H and C–O bonds was enhanced with increasing FeCl$_3$ dosage, suggesting that iron was beneficial to the external formation of oxygen-rich functional groups. Han et al. (2021) also found that relative to untreated biochar, the intensity of the peak assigned to aromatic C=O strengthened, which was attributed to Fe (III), enhancing the formation of aromatic structures in pyrochar and hydrochar.

The sequential responses of the functional groups in Fex@biochar to the FeCl$_3$ dosages were further analyzed using 2D FTIR COS maps. As shown in Fig. 1c, six main auto-peaks appear at 561, 1059, 1500, 1610, 2918, and 3451 cm^{-1} along the diagonal line. There were thirteen positive cross-peaks at (561, 1059), (561, 1610), (561, 2918), (561, 3451), (1059, 1610), (1059, 2918), (1059, 3451), (1500, 1610), (1500, 2918), (1500, 3451), (1610, 2918), (1610, 3451), and (2918, 3451) cm^{-1}, which suggested that the variation in Fe–O, aliphatic C–O–H, C–N, aromatic C=C or C=O, aliphatic C–H, and O–H in Fex@biochar showed the same trend with the increase in FeCl$_3$ dosages. As shown in asynchronous spectra (Fig. 1d), the signs of the other seven cross-peaks were positive, in addition to (1500, 1610), (1500, 2918), (1500, 3451), (1610, 2918), (1610, 3451), and (2918, 3451) cm^{-1}. According to Noda's rules (Noda et al., 1996), the sequential responses of the functional groups in Fex@biochar were 561, 1059, 3451, 2918, 1610, and 1500 cm^{-1} with increasing FeCl$_3$ dosage, that is, Fe–O stretching vibration → aliphatic C–O–H stretching vibrations → O–H stretching →

aliphatic C–H stretching vibration → aromatic C=C or C=O stretching vibration → C–N bending vibration. During pyrolysis, the internal water of the biomass first evaporated, engaged with iron on the surface of the biomass, hydrolyzed to Fe(OH)$_3$ and FeO(OH), and then decomposed into Fe$_2$O$_3$ (Yang et al., 2016; Hou et al., 2018). In this process, the reducing gases produced, such as CO and H$_2$, could also reduce Fe$_2$O$_3$ to FeO (Meng et al., 2013), resulting in the formation of Fe–O bonds in Fex@biochar during pyrolysis (Yang et al., 2007). Xu et al. (2021) also observed the peak of Fe–OH/Fe–O on the surface of Fe-biochar pyrolyzed by 400 °C and speculated that it was caused by the formation of amorphous iron hydroxide. The literature has proved that glucose and hemicellulose probably decomposed at lower pyrolysis temperatures, with glucose primarily losing weight at less than 200 °C and hemicellulose between 220 and 300 °C. Additionally, an increase in the FeCl$_3$ dosage significantly decreased the activation energy of the biomass, resulting in aromatic compounds being pyrolyzed in the low-temperature range (Ge et al., 2023). Thus, aliphatic C–O–H bonds in hemicellulose and cellulose, as well as the aliphatic C–H bonds, changed before the aromatic C=C or C=O. In summary, the FeCl$_3$ dosage significantly affected the formation of functional groups in Fex@biochar during pyrolysis, which was crucial for explaining the electrochemical properties of Fex@biochar and PS activation.

3.2. Major chemical structural components

To investigate the surface element composition, species, and quantities of the chemical structural components, we analyzed the C, O, and Fe elements in the Fex@biochar using XPS analysis and high-resolution spectra (Fig. 2a). The relative contents of C=C, -C-OH, -C=O, Fe(III) magnetite, Fe(II) (2p3/2), Fe(III) (2p1/2), and Fe2p1/2 in the Fex@biochar are shown in Fig. S3 and Table S2. The C=C content tended to increase and subsequently decrease with increasing FeCl₃ dosage, and it was the highest, reaching 69.24%, when the FeCl₃ dosage was 100 mM. The C=C content could characterize the degree of graphitization, suggesting that the range of 10–100 mM of FeCl₃ dosages was conducive to the formation of graphitized structures during pyrolysis (Meng et al., 2013). The intensity ratio of the D-band and G-band (I_D/I_G) was determined, and the values of Fe10@biochar ∼ Fe500@biochar were 1.09, 1.08, 1.07, 1.02, and 0.94 (Fig. 2b), which confirmed that the increase in Fe dosage contributed to the conversion of the carbon support from defective carbon to ordered graphitic carbon (Ren et al., 2022). The -C-OH content significantly decreased by 14.14% when the FeCl₃ dosage increased from 10 to 500 mM, which was caused by the thermal instability of the C–O bonds in -C-OH in the presence of excess iron, resulting

in the formation of –C=O (Fu et al., 2009). For Fe2p, with FeCl₃ dosages ranging from 10 to 500 mM, the relative contents of Fe(III) magnetite were 30.25%, 30.42%, 43.20%, 29.97%, and 34.27%. The average relative content of Fe(II) (2p3/2) was 24.52%, indicating the formation of Fe₃O₄ during pyrolysis (Karunanayake et al., 2019). Furthermore, when the FeCl₃ dosage increased from 10 to 500 mM, the Fe (III) (2p1/2) content decreased from 25.98% to 18.40%, and the contribution of Fe2p1/2 increased from 15.62% to 23.95%, respectively. Hence, Fe(III) (2p1/2) might be converted into Fe2p1/2 with increasing FeCl₃ dosage. These results illustrated that γ-Fe₂O₃ is the main iron species at low FeCl₃ dosages, whereas more Fe₃O₄ is formed at higher FeCl₃ dosages. The increase in the FeCl₃ dosage possibly decreased the potential barrier during pyrolysis and increased the temperature of the biomass surface, promoting the conversion of iron phases from low crystallinity to crystalline magnetite. A similar result showed that iron phases in biochar transformed into low-crystalline Fe₂O₃ under 400 °C and further converted into crystal magnetite (Fe₃O₄, FeO, and metallic-Fe) at a higher temperature (Xu et al., 2022). Moreover, the values of the vibration sample magnetometer of Fe10@biochar ∼ Fe500@biochar were 0.05, 0.14, 0.30, 0.89, and 1.09 A m²·kg⁻¹, respectively (Fig. S4), confirming that more Fe₃O₄ was formed at higher FeCl₃ dosages. In all, the contents
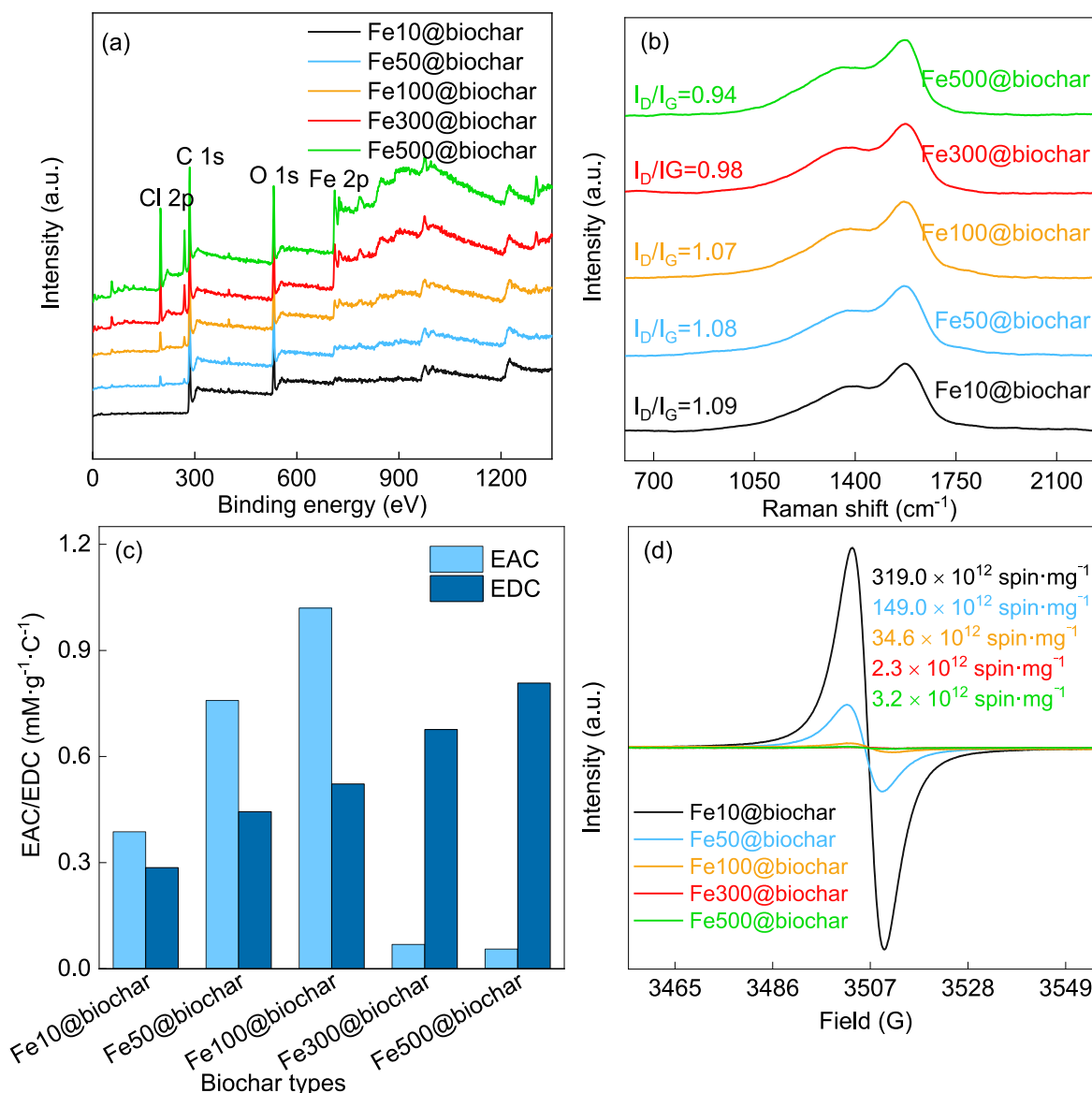

Fig. 2. XPS survey spectra (a); Raman spectra (b); EAC and EDC (c); and ESR spectra of oxygen vacancy (d) of Fex@biochar prepared by different FeCl₃ dosages.

of Fe(III) in Fe10@biochar ~ Fe500@biochar were 56.2%–67.1%, and the Fe (II) ranged from 32.9% to 49.8%.
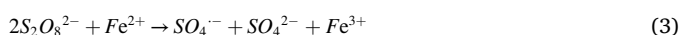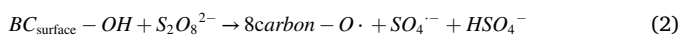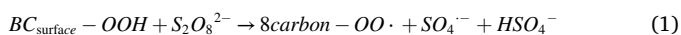
3.3. Electrochemical properties of biochar composite loaded with Fe

The electrochemical properties of Fex@biochar comprised those of EAC and EDC (Fig. 2c). With the increase in the $FeCl_3$ dosage from 10 to 500 mM, the EDC of Fex@biochar maintained a continually increasing trend (0.29–0.81 mM e$^-$/(g·C)). Liang et al. (2021) concluded from zeta potential analysis that the incorporated iron speciation changed the surface charge of biochar, and increasing the iron content might result in more positive charges in biochar. The EAC of Fex@biochar increased as the $FeCl_3$ dosage increased from 10 to 100 mM but decreased at 300 and 500 mM $FeCl_3$. The values were determined to be 0.39, 0.76, 1.02, 0.07, and 0.06 mM e$^-$/(g·C), possibly attributed to the higher Fe (III) and oxygen vacancies in the Fe10@biochar, Fe50@biochar, and Fe100@biochar than that of Fe300@biochar, and Fe500@biochar (Fig. 2d and Table S2). The oxygen vacancies were determined from the ESR spectra, and the values decreased by 1–2 orders of magnitude when the $FeCl_3$ dosage was increased from 10 mM to 300 and 500 mM. A study also reported that the oxygen vacancies of Fex@biochar were significantly higher than those of biochar, attributed to the increase in oxygen vacancies caused by an increase in surface defects after the interaction with iron (Liu et al., 2022). Correspondingly, the increase in oxygen vacancies improved the EAC of Fex@biochar. Therefore, appropriate $FeCl_3$ dosages are crucial for the preparation of Fex@biochar because they affect its electrochemical properties.

3.4. Persulfate activation performance by biochar composite loaded with Fe

3.4.1. Catalytic removal of 2,4-DNT in different systems

A comparison of the 2,4-DNT removal performance of the PS, Fe100@biochar, and PS/Fe100@biochar systems is shown in Fig. 3a. In the PS system, the 2,4-DNT removal rate was low (3.2% after 10 h of reaction), attributed to low activity of PS, and its weak oxidation capacity for organic contaminants (Ahmad et al., 2013). The removal rate for the Fe100@biochar system was 27.4% for 2,4-DNT (Fig. S5). This phenomenon was mainly attributed to adsorption by Fe100@biochar, but the adsorption capacity was limited owing to its low dosage. In the PS/Fe100@biochar system, the removal rate of 2,4-DNT reached 100% after 10 h of reaction. $S_2O_8^{2-}$ could be effectively activated by transition metal ions and oxygen functional groups in biochar, generating $SO_4^{\bullet-}$ (Eq. (1) ~ (3)). Furthermore, $SO_4^{\bullet-}$ reacted with OH^- to produce $\bullet OH$ (Eq. (4)) to degrade 2,4-DNT. Therefore, 2,4-DNT removal by the PS/Fe100@biochar system was significantly higher than that by the PS and Fe100@biochar systems. The leaching concentration of Fe ions in the PS/Fe100@biochar system was 0.006 mM (Fig. S6). In our previous study, when the concentrations of PS and Fe^{2+} were retained at 2.5 and 0.2 mM, respectively, 2,4-DNT removal was 30.3% after 9 h of reaction (Li et al., 2021). These results indicated that the concentration of dissolved Fe ions for 2,4-DNT removal was nonsignificant in the PS/Fex@biochar system. The XRD analysis showed that iron speciation occurred on the biochar after $FeCl_3$ impregnation and pyrolysis, and different iron speciation levels facilitated the electron transfer process on the Fex@biochar surface (Yan et al., 2017). Therefore, we reasonably speculated that certain iron species participated in the activation of PS and that combined with oxygen functional groups in Fex@biochar may exert synergistic effects on PS activation, discussed in sections 3.4 and 3.5.

$$BC_{surface} - OOH + S_2O_8{}^{2-} \rightarrow 8carbon - OO\cdot + SO_4{}^{\cdot-} + HSO_4{}^- \quad (1)$$

$$BC_{surface} - OH + S_2O_8{}^{2-} \rightarrow 8carbon - O\cdot + SO_4{}^{\cdot-} + HSO_4{}^- \quad (2)$$

$$2S_2O_8{}^{2-} + Fe^{2+} \rightarrow SO_4{}^{\cdot-} + SO_4{}^{2-} + Fe^{3+} \quad (3)$$

$$SO_4{}^{\cdot-} + OH^- \rightarrow SO_4{}^{2-} + \cdot OH \quad (4)$$

After 10 h of reaction, the removal rates of 2,4-DNT were 22.4%–27.9% in all Fex@biochar systems, suggesting that Fex@biochar has poor adsorption capacity for 2,4-DNT (Fig. S5). In the PS/Fe100 system (Fe100 represents the concentration of iron loading on the surface of Fe100@biochar when the $FeCl_3$ impregnation concentration is 100 mM), 21.4% of 2,4-DNT was removed, and the kinetic constant (k_{obs}) was determined to be 0.022 min^{-1}. The influence of the $FeCl_3$ dosage on PS activation by Fex@biochar is shown in Fig. 3b. 2,4-DNT removal visibly improved when the $FeCl_3$ dosage increased from 10 to 100 mM, and the time for complete removal of 2,4-DNT was reduced from 10 to 5 h. The pseudo-first-order reaction kinetics were well described by the 2,4-DNT removal ($R^2 > 0.90$), and k_{obs} increased from 0.341 to 1.363 min^{-1} (Fig. 3c). The XRD and FTIR analyses demonstrated that the contents of some iron species and functional groups (e.g., Fe(III) (2p1/2), –C=C/C–C) in Fex@biochar also increased with as the $FeCl_3$ dosage increased, which possibly served as active sites to activate PS, producing more free radicals (Wang et al., 2019). However, when $FeCl_3$ dosages increased to 300 mM and 500 mM, the k_{obs} values declined to 0.117 and 0.077 min^{-1} (Fig. 3c). The XPS analysis showed that the strength of Cl 2p increased as the $FeCl_3$ dosage increased, indicating that more Cl$^-$ was loaded on the surface of Fe300@biochar and Fe500@biochar (Fig. 2a). The effect of Cl$^-$ (0–10.0 mM) on 2,4-DNT removal by PS/Fe100@biochar was also investigated (Fig. S8a). When the concentration of Cl$^-$ was higher than 2.5 mM, the removal rate of 2,4-DNT decreased by 19.3%–49.7%. Therefore, we reasonably speculated that a high $FeCl_3$ content increases Cl$^-$ content in Fex@biochar, which might inhibit 2,4-DNT removal by the PS/Fe300@biochar and PS/Fe500@biochar systems. Moreover, the excessive Fe in Fex@biochar may act as an inducer to quench some of the reactive species, reducing the removal of contaminants (Deng et al., 2018; Hao et al., 2020). These results suggested that Fe100@biochar presented the best catalytic activity and was thus used as an activator for PS activation in the following experiments.

The effect of Fe100@biochar dosage on PS activation for 2,4-DNT removal was also investigated (Fig. 3d). As the Fe100@biochar dosages increased from 0.1 to 0.5 g/L, the 2,4-DNT removal gradually improved until it reached 100% after 5 h reaction at the dosage of 0.5 g/L. However, as the Fe100@biochar dosages increased from 0.5 to 0.8 and 1.0 g/L, the 2,4-DNT removal rate decreased to 94% and 90%. This result indicates that an appropriate dosage of Fex@biochar could improve the PS decomposition to remove organic pollutants without consuming the $SO_4^{\bullet-}$ and $\bullet OH$, improving the removal efficiency (Wei et al., 2022b).

3.4.2. Identification of reactive species

To verify the roles of high valent Fe(IV) and singlet oxygen ($^1O_2$) in the PS/Fe100@biochar system, we selected methyl phenyl sulfoxide (2.5 mM) and FA (2.5 mM), respectively to conduct the quenching experiment (Pan et al., 2021; Mo et al., 2023). As shown in Fig. 4a and S9, with 2.5 mM methyl phenyl sulfoxide, methyl phenyl sulfone was not detected during 2,4-DNT removal. In the FA system, the removal of 2,4-DNT was not inhibited after 5 h. The results indicated the Fe(IV) and $^1O_2$ did not produce in the PS/Fe100@biochar system. TBA ($k_{SO4}^{\bullet-} = 4.0 \times 10^5$ M^{-1} S^{-1}; $k_{\bullet OH} = 3.8 \times 10^8$ M^{-1} S^{-1}) and EtOH ($k_{SO4}^{\bullet-} = 1.6$–7.7×10^7 M^{-1} S^{-1}, $k_{\bullet OH} = 1.2$–2.8×10^9 M^{-1} S^{-1}) were used to identify the reactive species during 2,4-DNT removal by PS/Fex@biochar oxidation (Yang et al., 2020). As shown in Fig. 4a, when 0.5 or 2.5 mM TBA was transferred into the PS/Fe100@biochar system, the removal rate of 2,4-DNT reduced from 100% to 43.3% and 30.9% after a 5 h reaction, respectively. In the PS/Fe100@biochar system with 2.5 mM EtOH, the obvious inhibition of 2,4-DNT removal occurred, and the removal rate decreased to 15.8% after 5 h reaction, suggesting that $SO_4^{\bullet-}$ and $\bullet OH$ could degrade 2,4-DNT, but $\bullet OH$ played a major part in the PS/Fex@biochar system. The types and intensities of the reactive species were also analyzed using ESR spectra during 2,4-DNT removal (Fig. 4b). The
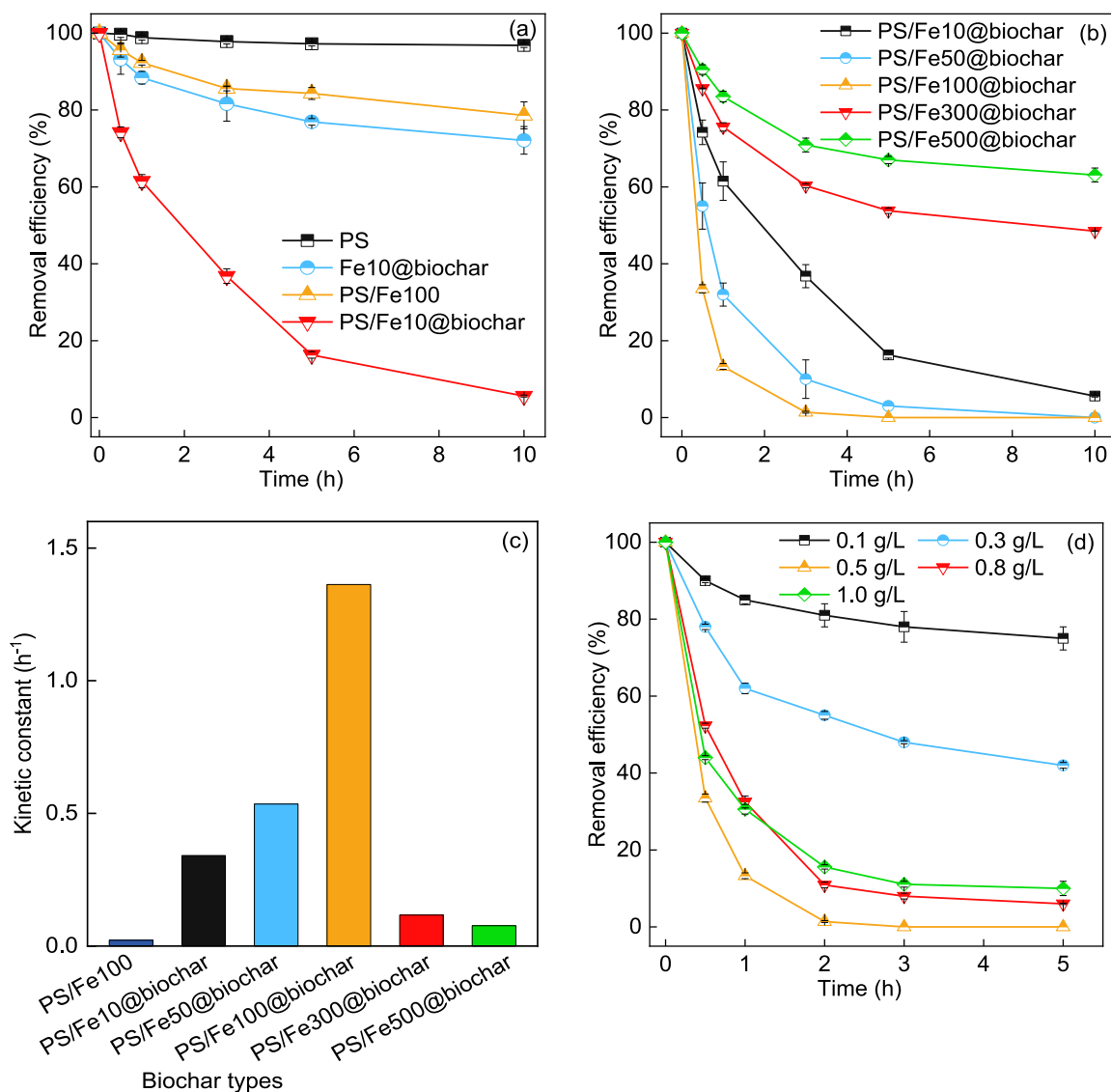
Fig. 3. 2,4-DNT removal rate of PS with and without Fe100@biochar (a); 2,4-DNT removal rate (b) and kinetic constants (c) of PS with different types of Fex@-biochar; Effect of Fe100@biochar dosages on 2,4-DNT removal (d) (except for the investigated parameters, the other parameters were fixed at: [2,4-DNT] = 14.0 μM, [PS] = 2.5 mM, [Fex@biochar] = 0.5 g/L, unadjusted pH (4.05)).
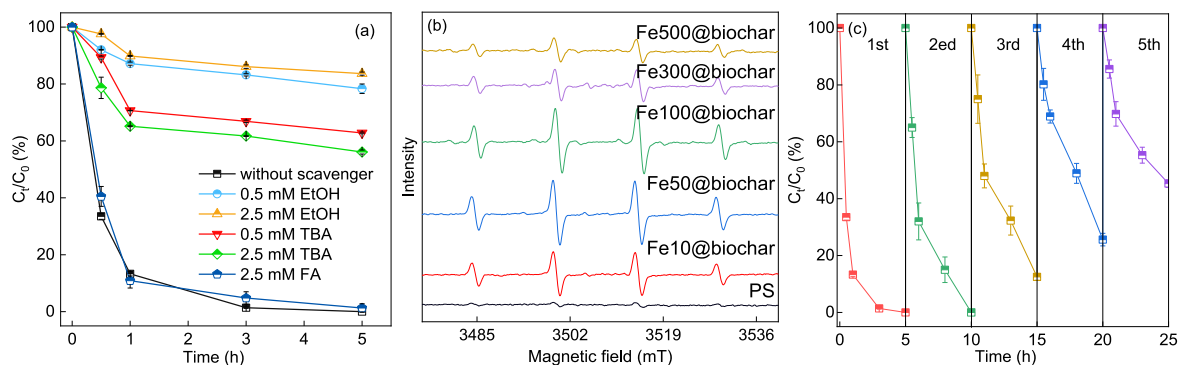

Fig. 4. Effect of radical scavengers on 2,4-DNT removal (a); ESR spectra with different PS/Fex@biochar systems (b); long-term 2,4-DNT removal of PS with Fe100@biochar system (c) ([2,4-DNT] = 14.0 μmol/L, [PS] = 2.5 mmol/L, [Fex@biochar] = 0.5 g/L, unadjusted pH (4.05)).

intensity of $SO_4^{\bullet-}$ and $\bullet OH$ in the PS/Fex@biochar system first increased and subsequently decreased with an increase in $FeCl_3$ dosage, indicating that an appropriate $FeCl_3$ dosage in Fex@biochar is beneficial for activating PS and generating substantial free radicals.

3.4.3. Implications for sustainable utilization and practicability

Cycling tests were performed to evaluate the reusability of Fe100@biochar for PS activation (Fig. 4c). From the first to the fifth experiments, the 2,4-DNT removal rates were 100%, 100%, 87.5%, 72.3%, and 56.3%, respectively, after 5 h of reaction. The reduction in 2,4-DNT removal might be due to partial iron leaching into the solution, resulting in a decrease in iron in Fe100@biochar (Deng et al., 2018). Moreover, the adsorption of 2,4-DNT and its degradation products could also reduce the catalytic ability of Fe100@biochar (Hao et al., 2020). This result provides supportive evidence that Fe100@biochar exhibits excellent performance in PS activation and has good stability and reusability. The reasonable use of Fex@biochar has the potential benefits of a circular economy and is favorable for carbon neutrality through its carbon sequestration properties (He et al., 2022a).

3.5. Relationships between chemical structural components, electrochemical properties, and kinetic constant of 2,4-DNT removal

The potential correlations among the chemical structural components of Fex@biochar, the electrochemical properties of Fex@biochar, and the kinetic constant of 2,4-DNT removal in the PS/Fex@biochar system was performed using Origin version 2022 (Fig. 5). The positive correlation is filled in red, the negative correlation is filled in blue, and the shade symbolizes the degree of correlation. The EAC of the Fex@-biochar showed an extremely significant positive correlation with Fe (III) content (R = 0.90, $p < 0.05$). A higher content of Fe (III) promoted the EAC and restrain the EDC of Fex@biochar, which was caused by the strong EAC of Fe (III) (Zeng et al., 2021). The EDC of Fex@biochar showed a significant negative correlation with O–C=O, I_D/I_G, and oxygen vacancy (R > −0.89, $p < 0.05$). Oxygen vacancy was produced by O atoms of metal oxides leaving the lattice and was one of the defective structures (Zhang et al., 2016a; Rasi et al., 2023), which was positively charged and had a local electron deficiency state (He et al., 2022b), hence it was negatively correlated with the EDC. The I_D/I_G showed a significant positive correlation with Fe (III) (2p1/2) (R = 0.99, $p < 0.01$) and a negative correlation with Fe2p1/2, suggesting that conversion of Fe2p1/2 to Fe (III) (2p1/2) possibly occurred in the vicinity of the defects. Similarly, a significant correlation of I_D/I_G with O–C=O (R = 0.98,

$p < 0.01$), C=O (R = −0.93, $p < 0.01$), and C–O–C/C–OH (R = −0.88, $p < 0.05$) were also observed in Fig. 5, suggesting that the conversion of C=O and C–O–C/C–OH functional groups to O–C=O may occur near the defect location. Moreover, a positive correlation (R = 0.98, $p < 0.01$) between Fe (III) (2p1/2) and O–C=O was observed, suggesting the synergistic effect between the generation of Fe (III) (2p1/2) and O–C=O during pyrolysis. Therefore, we speculated that the changes of defect structure caused the transformation of surface functional groups and Fe species, which affected the EDC and EAC of Fex@biochar. These results indicated during pyrolysis of Fex@biochar, $FeCl_3$ dosage affected the EAC by controlling Fe (III) content, and the EDC through changing the contents of O–C=O, I_D/I_G, and oxygen vacancy.

More importantly, the kinetic constant of 2,4-DNT removal was significantly correlated with EAC and Fe (III) (R > 0.93, $p < 0.05$), indicating that the changes in Fe (III) content altered the EAC in the PS/Fex@biochar system, further dominating PS activation and 2,4-DNT removal. Our result differs from that of a study reporting that the EDC of biochar showed a positive correlation with the kinetic constant of phenol removal in the PS/biochar/Fe^{2+} system (Zeng et al., 2021). In this study, we assumed that the EDC showed an increasing trend as the $FeCl_3$ dosage increased during pyrolysis, but the Fe (III) content in the Fex@biochar was altered, leading to an initial increase followed by a decreasing trend in the EAC values (Table S2), which limited the velocity of the redox cycle and dominated PS activation.

3.6. Catalysis mechanism analysis

The mechanism of 2,4-DNT removal in the PS/Fex@biochar system was proposed in this study (Fig. 6). From the perspective of 2,4-DNT removal, Fex@biochar plays a dual role (adsorption and PS activation) due to its substantial specific surface area (4.2–16.6 m^2 g^{-1}) and abundance of reactive sites (Figs. 1 and 2). After a 10 h reaction, the adsorption of Fex@biochar contributed 22.4%–27.9% to 2,4-DNT removal (Fig. S5). The previous studies affirmed that the adsorption performance of Fe100@biochar included the intermolecular interaction between contaminants and active sites, as well as physical activity, such as $\pi-\pi$ interaction, a hydrogen bond, an electrostatic interaction, ion exchange, or pore filling (Li et al., 2020b; Hassan et al., 2022). More importantly, how Fex@biochar directly activates PS and thereby causes a high efficiency of 2,4-DNT degradation should be investigated. In our case, a significant positive correlation was observed among the kinetic constants of 2,4-DNT removal, EAC, and Fe (III) content (R = 0.90, $p < 0.05$, Fig. 5). We concluded that $FeCl_3$ impregnation concentration controlled the Fe (III) content on the surface of Fex@biochar, which further altered the EAC in the PS/Fex@biochar system and dominated PS activation and 2,4-DNT removal. To further revealed the catalysis mechanism of PS activation with Fe100@biochr for 2,4-dinitrotoluene degradation, the XPS and FTIR were used to characterize the Fe100@biochar after the reaction. As shown in Fig. S10, the content of Fe2p1/2 and Fe(II) (2p3/2) were decreased by 6.7% and 4.4%, which indicated Fe(II) (2p3/2) is the main active substance of Fe species to activate PS. Yao et al. (2022) reported that electrons have transferred from Fe(II) to PS to generate reactive species. The FTIR spectra showed that the peak positions of the functional groups in Fe100@biochar were displaced, and the peak intensity decreased to varying degrees after the reaction (Fig. S11), indicating that functional groups, including O–H, C=O, and Fe–O, possibly participated in the reaction during PS/Fe100@biochar oxidation (Li et al., 2020c). Rong et al. (2019) speculated that C=O possibly participated in the PS activation process acted as the catalytic site, and it was oxidized to O–C=O during activation. The results indicated that Fe (II) and oxygen functional groups played a vital role in PS activation to produce $SO_4^{\bullet-}$ and $\bullet OH$.
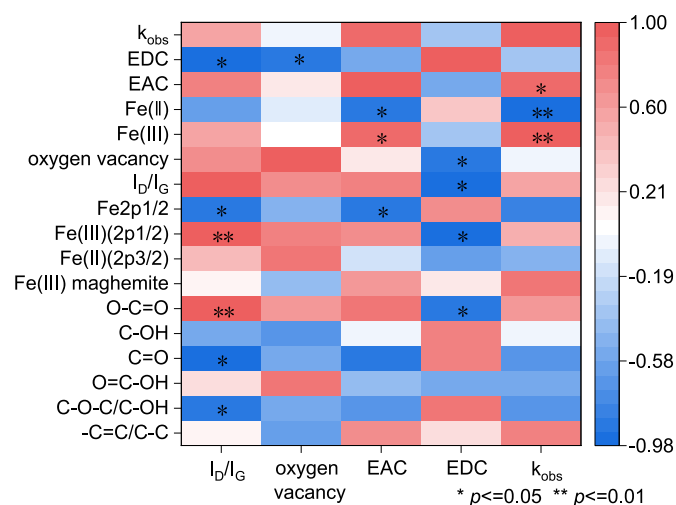

Fig. 5. Correlation coefficients between the chemical structural components, electrochemical properties, and kinetic constant of 2,4-DNT removal (*$p <$ 0.05, **$p < 0.01$).

4. Conclusion

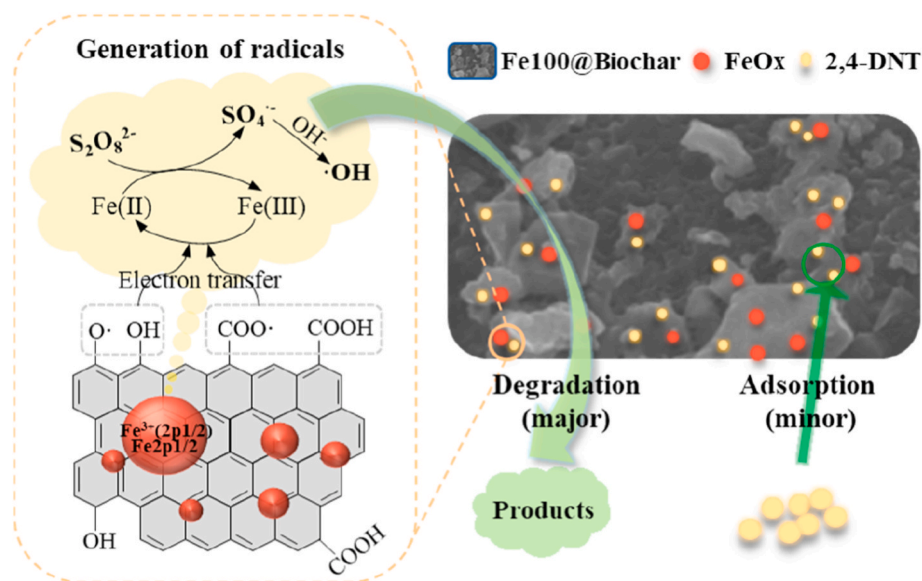With increasing $FeCl_3$ dosage, iron speciation in Fex@biochar

Fig. 6. The catalysis mechanism of PS activation with Fex@biochar for 2,4-DNT removal.

changed from γ-Fe_2O_3 to Fe_3O_4, and the variation in functional groups was as follows: Fe–O, aliphatic C–O–H, O–H, aliphatic C–H, aromatic C=C or C=O, and C–N. The EAC of Fex@biochar increased as the $FeCl_3$ dosage increased from 10 to 100 mM but decreased at 300 and 500 mM $FeCl_3$. 2,4-dinitrotoluene removal first increased and subsequently decreased, reaching 100% in the PS/Fe100@biochar system. The Fe100@biochar also showed good stability and reusability for PS activation, verified by five test cycles. The Pearson correlation coefficient and ESR analysis indicated that iron dosage altered the Fe (III) content and electron accepting capacity of Fex@biochar during pyrolysis, further controlling PS activation and 2,4-DNT removal. The results illustrated that the novel biochar composite loaded with Fe would be a potential PS catalyst for the degradation of refractory organic pollutants.

Credit author statement

Xiaodong Li: contributed to the experimental planning, experimental measurements, data analysis, and manuscript preparation. **Huizhen Cao**: contributed to the conceptualization, supervision, experimental planning, data analysis, and manuscript preparation. **Yuan Cao**: contributed to experimental measurements and data analysis. **Yao Zhao:** contributed to data analysis. **Wenwen Zhang**: conducted experimental measurements. **Jialun Shen**: conducted experimental measurements. **Zongquan Sun**: contributed to data curation, writing-review & editing. **Fujun Ma**: contributed to the conceptualization, supervision, experimental planning, data analysis, and manuscript preparation. **Qingbao Gu**: contributed to data curation, writing-review & editing, project administration, experimental planning, and funding acquisition.

Declaration of competing interest

The authors declare that they have no known competing financial interests or personal relationships that could have appeared to influence the work reported in this paper.

Data availability

The data that has been used is confidential.

Appendix A. Supplementary data

Supplementary data to this article can be found online at https://doi.org/10.1016/j.jenvman.2023.117955.

References

Ahmad, M., Teel, A.L., Watts, R.J., 2013. Mechanism of persulfate activation by phenols. Environ. Sci. Technol. 47, 5864–5871.
Amaral, H.I.F., Fernandes, J., Berg, M., Schwarzenbach, R.P., Kipfer, R., 2009. Assessing TNT and DNT groundwater contamination by compound-specific isotope analysis and ^{3}H-^{3}He groundwater dating: a case study in Portugal. Chemosphere 77, 805–812.
Bokare, A.D., Choi, W., 2014. Review of iron-free Fenton-like systems for activating H_2O_2 in advanced oxidation processes. J. Hazard Mater. 275, 121–135.
Deng, J., Dong, H., Zhang, C., Jiang, Z., Cheng, Y., Hou, K., Zhang, L., Fan, C., 2018. Nanoscale zero-valent iron/biochar composite as an activator for Fenton-like removal of sulfamethazine. Sep. Purif. Technol. 202, 130–137.
Fang, G., Liu, C., Gao, J., Dionysiou, D.D., Zhou, D., 2015. Manipulation of persistent free radicals in biochar to activate persulfate for contaminant degradation. Environ. Sci. Technol. 49, 5645–5653.
Fu, P., Hu, S., Sun, L., Xiang, J., Yang, T., Zhang, A., Zhang, J., 2009. Structural evolution of maize stalk/char particles during pyrolysis. Bioresour. Technol. 100, 4877–4883.
Ge, L.H., Zhao, C., Zuo, M.J., Du, Y.Y., Tang, J., Chu, H.Q., Wang, Y., Xu, G., 2023. Effects of Fe addition on pyrolysis characteristics of lignin. cellulose hemicellulose 107, 101177.
Guo, J., Jia, X., Gao, Q., 2020. Insight into the improvement of dewatering performance of waste activated sludge and the corresponding mechanism by biochar-activated persulfate oxidation. Sci. Total Environ. 744, 140912.
Guo, L., Zhao, L., Tang, Y., Zhou, J., Shi, B., 2022. An iron-based biochar for persulfate activation with highly efficient and durable removal of refractory dyes. J. Environ. Chem. Eng. 10, 106979.
Han, L.F., Sun, H.R., Sun, K., Yan, Y., Fang, L.P., Xing, B.S., 2021. Effect of Fe and Al ions on the production of biochar from agricultural biomass: properties, stability and adsorption efficiency of biochar. Renew. Sustain. Energy Rev. 145, 111133.
Hao, H., Zhang, Q., Qiu, Y., Meng, L., Tao, J., 2020. Insight into the degradation of Orange G by persulfate activated with biochar modified by iron and manganese oxides: synergism between Fe and Mn. J. Water Process Eng. 37, 101470.
Hassan, M., Du, J., Liu, Y., Naidu, R., Zhang, J., Ahsan, M.A., Qi, F., 2022. Magnetic biochar for removal of perfluorooctane sulphonate (PFOS): interfacial interaction and adsorption mechanism. Environ. Technol. Innov. 28, 102593.

He, M., Xu, Z.B., Hou, D.Y., Gao, B., Cao, X.D., Ok, Y.S., Rinklebe, J., Bolan, N., Tsang, D. C.W., 2022a. Waste-derived biochar for water pollution control and sustainable development. Nat. Rev. Earth Environ. 3, 444–460.

He, T., Liu, Z., Zhou, W., Cheng, X., He, L., Guang, Q., Zhou, H., 2022b. Constructing the vacancies and defects by hemp stem core alkali extraction residue biochar for highly effective removal of heavy metal ions. J. Environ. Manag. 323, 116256.

He, X., Lu, H., Wu, C., Xu, R., 2022c. Effects of inorganic alkalis and organic anions in biochars on acidic paddy soil resistance to acidification. J. Soils Sediments 22, 1201–1213.

Hou, T., Sun, X., Xie, D., Wang, M., Fan, A., Chen, Y., Cai, S., Zheng, C., Hu, W., 2018. Mesoporous graphitic carbon-encapsulated Fe_2O_3 nanocomposite as high-rate anode material for sodium-ion batteries. Chem. Eur. J. 24, 14786–14793.

Karunanayake, A.G., Navarathna, C.M., Gunatilake, S.R., Crowley, M., Anderson, R., Mohan, D., Perez, F., Pittman, C.U., Mlsna, T., 2019. Fe_3O_4 nanoparticles dispersed on douglas fir biochar for phosphate sorption. ACS Appl. Nano Mater. 2, 3467–3479.

Li, S., Shao, L., Zhang, H., He, P., Lu, F., 2020a. Quantifying the contributions of surface area and redox-active moieties to electron exchange capacities of biochar. J. Hazard Mater. 394, 122541.

Li, T., He, Y., Peng, X., 2020b. Efficient removal of tetrabromobisphenol A (TBBPA) using sewage sludge-derived biochar: adsorptive effect and mechanism. Chemosphere 251, 126370.

Li, T.T., Song, F.H., Bai, Y.C., Wu, F.C., Ruan, M.Q., Cao, Y.H., Zhou, L.F., Sun, F.H., 2023. Real-time emission, chemical properties, and dynamic evolution mechanism of volatile organic compounds during co-pyrolysis of rice straw and semi-bituminous coal. ACS EST Eng. https://doi.org/10.1021/acsestengg.2c00391.

Li, X.D., Shen, J.L., Sun, Z.Q., Liu, Y.Q., Zhang, W.W., Wu, B., Ma, F.J., Gu, Q.B., 2021. Degradation of 2,4-dinitrotoluene using ferrous activated persulfate: kinetics, mechanisms, and effects of natural water matrices. J. Environ. Chem. Eng. 5, 106048.

Li, Z., Sun, Y., Yang, Y., Han, Y., Wang, T., Chen, J., Tsang, D.C.W., 2020c. Biochar-supported nanoscale zero-valent iron as an efficient catalyst for organic degradation in groundwater. J. Hazard Mater. 383, 121240.

Liang, J., Duan, X., Xu, X., Chen, K., Zhang, Y., Zhao, L., Qiu, H., Wang, S., Cao, X., 2021. Persulfate oxidation of sulfamethoxazole by magnetic iron-char composites via nonradical pathways: Fe(IV) versus surface-mediated electron transfer. Environ. Sci. Technol. 55, 10077–10086.

Ling, L., Zhang, W., 2017. Visualizing arsenate reactions and encapsulation in a single zero-valent iron nanoparticle. Environ. Sci. Technol. 51, 2288–2294.

Liu, H., Ye, C., Xu, Y., Wang, Q., 2022. Effect of activation conditions and iron loading content on the catalytic cracking of toluene by biochar. Energy 247, 123409.

Lyu, H., Tang, J., Cui, M., Gao, B., Shen, B., 2020. Biochar/iron (BC/Fe) composites for soil and groundwater remediation: synthesis, applications, and mechanisms. Chemosphere 246, 125609.

Meng, A., Zhou, H., Qin, L., Zhang, Y., Li, Q., 2013. Quantitative and kinetic TG-FTIR investigation on three kinds of biomass pyrolysis. J. Anal. Appl. Pyrolysis 104, 28–37.

Mo, Z.H., Tan, Z.X., Jiang, J.L., Zhang, L., Li, C.J., Huang, S.S., Sun, S.Y., Sun, Y., 2023. Iron-rich digestate biochar toward sustainable peroxymonosulfate activation for efficient anaerobic digestate dewaterability. J. Hazard Mater. 443, 130200.

Noda, I., Liu, Y.L., Ozaki, Y., 1996. Two-dimensional correlation spectroscopy study of temperature-dependent spectral variations of N-methylacetamide in the pure liquid state. 2. Two-dimensional Raman and infrared-Raman heterospectral analysis. J. Phys. Chem. 100, 8674–8680.

Niznansky, D., Viart, N., Rehspringer, J.L., 1997. Nanocomposites Fe_2O_3/SiO_2-preparation by sol-gel method and physical properties. J. Sol. Gel Sci. Technol. 8, 615–618.

Pan, L.H., Shi, W., Sen, T., Wang, L.Z., Zhang, J.L., 2021. Visible light-driven selective organic degradation by $FeTiO_3$/persulfate system: the formation and effect of high valent Fe(IV). Appl. Catal. B Environ. 2021 (280), 119414.

Poulson, S.R., Naraoka, H., 2002. Carbon isotope fractionation during permanganate oxidation of chlorinated ethylenes (cDCE, TCE, PCE). Environ. Sci. Technol. 36, 3270–3274.

Rasi, N.M., Ponnurangam, S., Mahinpey, N., 2023. First-principles investigations into the effect of oxygen vacancies on the enhanced reactivity of NiO via Bader charge and density of states analysis. Catal. Today 407, 172–181.

Ren, Z.J., Wang, Z.X., Lv, L.Y., Ma, P.Y., Zhang, G.M., Li, Y.Y., Qin, Y., Wang, P.F., Liu, X. Y., Gao, W.F., 2022. Fe-N complex biochar as a superior partner of sodium sulfide for methyl orange decolorization by combination of adsorption and reduction. J. Environ. Manag. 316, 115213.

Rong, X., Xie, M., Kong, L.S., Natarajan, V., Ma, L., Zhan, J.H., 2019. The magnetic biochar derived from banana peels as a persulfate activator for organic contaminants degradation. Chem. Eng. J. 372, 294–303.

Ruan, M.Q., Wu, F.C., Sun, F.H., Song, F.H., Li, T.T., He, C., Jiang, J., 2023. Molecular-level exploration of properties of dissolved organic matter in natural and engineered water systems: a critical review of FTICR-MS application. Crit. Rev. Environ. Sci. Technol. https://doi.org/10.1080/10643389.2022.2157167.

Song, F., Li, T., Shi, Q., Guo, F., Bai, Y., Wu, F., Xing, B., 2021a. Novel insights into the molecular-level mechanism linking the chemical diversity and copper binding heterogeneity of biochar-derived dissolved black carbon and dissolved organic matter. Environ. Sci. Technol. 55, 11624–11636.

Song, F., Li, T., Zhang, J., Wang, X., Bai, Y., Giesy, J.P., Xing, B., Wu, F., 2019. Novel insights into the kinetics, evolved gases and mechanisms for biomass (sugar cane residue) pyrolysis. Environ. Sci. Technol. 53, 13495–13505.

Song, G., Qin, F.Z., Yu, J.F., Tang, L., Pang, Y., Zhang, C., Wang, J.J., Deng, L.F., 2021b. Tailoring biochar for persulfate-based environmental catalysis: impact of biomass feedstocks. J. Hazard Mater. 424, 127663.

Sun, Z., Feng, L., Li, Y., Han, Y., Zhou, H., Pan, J., 2022a. The role of electrochemical properties of biochar to promote methane production in anaerobic digestion. J. Clean. Prod. 362, 132296.

Sun, Y.Q., Yu, I.K.M., Tsang, D.C.W., Cao, X.D., Lin, D.H., Wang, L.L., Graham, N.J.D., Alessi, D.S., Komárek, M., Ok, Y.S., Feng, Y.J., Li, X.D., 2019. Multifunctional iron-biochar composites for the removal of potentially toxic elements, inherent cations, and hetero-chloride from hydraulic fracturing wastewater. Environ. Int. 124, 521–532.

Sun, Y.Q., Zhang, Q.Z., Clark, J.H., Graham, N.J.D., Hou, D.Y., Ok, Y.S., Tsang, D.C.W., 2022b. Tailoring wood waste biochar as a reusable microwave absorbent for pollutant removal: structure-property-performance relationship and iron-carbon interaction. Bioresour. Technol. 362, 127838.

Wang, B., Li, Y., Wang, L., 2019. Metal-free activation of persulfates by corn stalk biochar for the degradation of antibiotic norfloxacin: activation factors and degradation mechanism. Chemosphere 237, 124454.

Wang, C., Huang, R., Sun, R., Yang, J., Sillanp, M., 2021. A review on persulfates activation by functional biochar for organic contaminants removal: synthesis, characterizations, radical determination, and mechanism. J. Environ. Chem. Eng. 9, 106267.

Wang, K., Sun, Y., Tang, J., He, J., Sun, H., 2020. Aqueous Cr(VI) removal by a novel ball milled Fe^0-biochar composite: role of biochar electron transfer capacity under high pyrolysis temperature. Chemosphere 241, 125044.

Wang, M.M., Wang, Y.F., Li, Y.C., Wang, C.H., Kuang, S.P., Ren, Peng, Xie, B.H., 2023. Persulfate oxidation of tetracycline, antibiotic resistant bacteria, and resistance genes activated by Fe doped biochar catalysts: synergy of radical and nonradical processes. Chem. Eng. J. https://doi.org/10.1016/j.cej. 2023.142558.

Wei, K., Ma, J., Xi, B., Yu, M., Cui, J., Chen, B., Li, Y., Gu, Q., He, X., 2022a. Recent progress on in-situ chemical oxidation for the remediation of petroleum contaminated soil and groundwater. J. Hazard Mater. 432, 128738.

Wei, T.Q., Meng, Y., Ai, D., Zhu, C., Wang, B., 2022b. Ball milling Fe_3O_4@biochar cathode coupling persulfate for the removal of sulfadiazine from water: effectiveness and mechanisms. J. Environ. Chem. Eng. 10, 108879.

Xing, X., Fan, F., Jiang, W., 2018. Characteristics of biochar pellets from corn straw under different pyrolysis temperatures. R. Soc. Open Sci. 5, 172346.

Xu, Z., Wan, Z., Sun, Y., Cao, X., Hou, D., Alessi, D.S., Ok, Y.S., Tsang, D.C.W., 2021. Unraveling iron speciation on Fe-biochar with distinct arsenic removal mechanisms and depth distributions of as and Fe. Chem. Eng. J. 425, 131489.

Xu, Z., Wan, Z., Sun, Y., Gao, B., Hou, D., Cao, X., Komárek, M., Ok, Y.S., Tsang, D.C.W., 2022. Electroactive Fe-biochar for redox-related remediation of arsenic and chromium: distinct redox nature with varying iron/carbon speciation. J. Hazard Mater. 430, 128479.

Yan, J., Qian, L., Gao, W., Chen, Y., Ouyang, D., Chen, M., 2017. Enhanced Fenton-like degradation of trichloroethylene by hydrogen peroxide activated with nanoscale zero valent iron loaded on biochar. Sci. Rep. 7, 43051.

Yang, F., Jiang, Y., Dai, M., Hou, X., Peng, C., 2022. Active biochar-supported iron oxides for Cr(VI) removal from groundwater: kinetics, stability and the key role of FeO in electron-transfer mechanism. J. Hazard Mater. 424, 127542.

Yang, H., Yan, R., Chen, H., Lee, D.H., Zheng, C., 2007. Characteristics of hemicellulose, cellulose and lignin pyrolysis. Fuel 86, 1781–1788.

Yang, J., Zhao, Y., Ma, S., Zhu, B., Zhang, J., Zheng, C., 2016. Mercury removal by magnetic biochar derived from simultaneous activation and magnetization of sawdust. Environ. Sci. Technol. 50, 12040–12047.

Yang, L., Chen, Y., Ouyang, D., Yan, J., Qian, L., Han, L., Chen, M., Li, J., Gu, M., 2020. Mechanistic insights into adsorptive and oxidative removal of monochlorobenzene in biochar-supported nanoscale zero-valent iron/persulfate system. Chem. Eng. J. 400, 125811.

Yao, B., Luo, Z.R., Du, S.Z., Yang, J., Zhi, D., Zhou, Y.Y., 2022. Magnetic $MgFe_2O_4$/biochar derived from pomelo peel as a persulfate activator for levofloxacin degradation: effects and mechanistic consideration. Bioresour. Technol. 346, 126547.

Yi, Y., Tu, G., Tsang, P.E., Fang, Z., 2020. Insight into the influence of pyrolysis temperature on Fenton-like catalytic performance of magnetic biochar. Chem. Eng. J. 380, 122518.

Yu, M., Shang, J., Kuang, Y., 2021. Efficient photocatalytic reduction of chromium (VI) using photoreduced graphene oxide as photocatalyst under visible light irradiation. J. Mater. Sci. Technol. 91, 17–27.

Yuan, J., Xu, R., Zhang, H., 2011. The forms of alkalis in the biochar produced from crop residues at different temperatures. Bioresour. Technol. 102, 3488–3497.

Zeng, L., Chen, Q., Tan, Y., Lan, P., Zhou, D., Wu, M., Liang, N., Pan, B., Xing, B., 2021. Dual roles of biochar redox property in mediating 2,4-dichlorophenol degradation in the presence of Fe^{3+} and persulfate. Chemosphere 279, 130456.

Zhang, R., Zheng, X., Chen, B., Ma, J., Niu, X., Zhang, D., Lin, Z., Fu, M., Zhou, S., 2020. Enhanced adsorption of sulfamethoxazole from aqueous solution by Fe-impregnated graphited biochar. J. Clean. Prod. 256, 120662.

Zhang, N., Li, X., Ye, H., Chen, S., Ju, H., Liu, D., Lin, Y., Ye, W., Wang, C., Xu, Q., 2016a. Oxide defect engineering enables to couple solar energy into oxygen activation. J. Am. Chem. Soc. 138, 8928–8935.

Zhang, X., Damacharla, D., Ma, D., Qi, Y., Tagett, R., Draghici, S., Kowluru, A., Yi, Z., 2016b. Quantitative proteomics reveals novel protein interaction partners of PP2A catalytic subunit in pancreatic β-cells. Mol. Cell. Endocrinol. 424, 1–11.